

Prethermal fragmentation in a periodically driven Fermionic chain

Somsubhra Ghosh¹, Indranil Paul², and K. Sengupta¹

¹*School of Physical Sciences, Indian Association for the Cultivation of Science, Kolkata 700032, India*

²*Université Paris Cité, CNRS, Laboratoire Matériaux et Phénomènes Quantiques, 75205 Paris, France*

(Dated: December 9, 2022)

We study a Fermionic chain with nearest-neighbor hopping and density-density interactions, where the nearest-neighbor interaction term is driven periodically. We show that such a driven chain exhibits prethermal strong Hilbert space fragmentation (HSF) in the high drive amplitude regime at specific drive frequencies ω_m^* . This constitutes the first realization of HSF for out-of-equilibrium systems. We obtain analytic expressions of ω_m^* using a Floquet perturbation theory and provide exact numerical computation of entanglement entropy, equal-time correlation functions, and the density autocorrelation of Fermions for finite chains. All of these quantities indicate clear signatures of strong HSF. We study the fate of the HSF as one tunes away from ω_m^* and discuss the extent of the prethermal regime as a function of the drive amplitude.

Eigenstate thermalization hypothesis (ETH) conjectures that mid-spectrum eigenstates of an isolated quantum system are locally thermal¹⁻⁴. A similar thermal characteristic leading to an infinite temperature steady state is seen for periodically driven systems^{5,6}. In both cases, ETH has been immensely successful in predicting the long-time dynamical behavior of local operators of isolated quantum systems. However, for periodically driven systems experimentally relevant time scales may be significantly shorter than their thermalization times⁷⁻⁹. In such cases, the prethermal characteristics of the driven system becomes relevant. It is well-known that these prethermal phases may exhibit interesting phenomena that have no equilibrium analogue⁹⁻¹⁸.

The violation of ETH in a quantum system comes primarily from the loss of ergodicity. This can occur in integrable quantum systems^{3,4} or in systems with strong disorder in their many body localized phases^{8,19,20}. In addition, a weak violation of ETH can also occur for many-body Hamiltonians hosting quantum scars²¹⁻²⁵ which may lead to long-time prethermal oscillatory dynamics, instead of ETH predicted rapid thermalization, of local correlation functions for certain initial states. The effect of the presence of such scars in the Floquet Hamiltonian of periodically driven systems has also been studied^{17,18,26,27}.

Another route to ETH violation in a quantum system occurs from fragmentation of its Hilbert space due to the presence of kinetic constraints on the dynamics of its constituent particles or spins²⁸⁻³⁷. The Hamiltonian of such a system, in the computational basis, breaks down into several dynamically disconnected blocks. For strong Hilbert space fragmentation (HSF), the number of such blocks increases exponentially with the system size; this is in sharp contrast to algebraic scaling of number of disconnected symmetry sectors. All the studies of strong HSF, so far, have involved equilibrium Hamiltonians; to the best of our knowledge, there has been no example of the existence of strong HSF in out-of-equilibrium quantum systems. In this work we provide the first example of prethermal HSF in a periodically driven Fermi chain with large drive amplitude at special drive frequencies.

To this end, we consider a Fermion chain with a Hamiltonian given by $H(t) = H_0(t) + H_1$

$$H_0(t) = V(t) \sum_{j=1..L} \hat{n}_j \hat{n}_{j+1} \quad (1)$$

$$H_1 = \sum_{j=1..L} -J(c_j^\dagger c_{j+1} + \text{h.c.}) + \hat{n}_j (V_0 \hat{n}_{j+1} + V_2 \hat{n}_{j+2})$$

where c_j denotes the Fermion annihilation operator for the site j of the chain, $\hat{n}_j = c_j^\dagger c_j$ is the Fermion density operator, $V_0 + V(t)$ and V_2 are the strengths of nearest- and next-nearest neighbor interactions respectively. In what follows, we drive this Fermion chain by making $V(t)$ a periodic function of time characterized by an amplitude $V_1 \gg V_0, J, V_2$ and frequency $\omega_D = 2\pi/T$, where T is the time period of the drive. The precise form of $V(t)$ depends on the drive protocol; in this letter we shall study both continuous cosine ($V(t) = V_1 \cos \omega_D t$) and discrete square-pulse ($V(t) = -(+)V_1$ for $t \leq (>)T/2$) protocols.

The results obtained from the study of such a Hamiltonian are as follows. First, we derive the Floquet Hamiltonian of the driven chain in the high amplitude limit using Floquet perturbation theory (FPT). We show that at special drive frequencies $\omega_D = \omega_m^*$, whose analytic expression we provide, the first order Floquet Hamiltonian, $H_F^{(1)}$, of the system reduces to a Fermionic model with constrained hopping which is known to exhibit HSF^{31,32}. In the high-drive amplitude regime, the higher order correction to $H_F^{(1)}$ are small; consequently, the driven system exhibits signatures of fragmentation over a long prethermal regime. Second, using exact diagonalization (ED), we compute exact evolution of the half-chain von-Neumann entanglement entropy, $S(nT)$, starting from a random Fock state, as a function of the number of drive cycles n . We find that away from ω_m^* , $S(nT)$ reaches the symmetry resolved Page value, S_p , as expected for non-integrable ergodic driven systems³⁸; in contrast, at $\omega_D = \omega_m^*$ and for large V_1 , $S(nT)$ saturates to the Page value, S_p^f , of the Hilbert space fragment of $H_F^{(1)}$ to which the initial state belongs for a long range of n . Third, we

compute the Fermion density autocorrelation function

$$C_j(nT) = \langle \psi_0 | (\hat{n}_j(nT) - 1/2)(\hat{n}_j(0) - 1/2) | \psi_0 \rangle \quad (2)$$

starting from a random infinite-temperature initial state $|\psi_0\rangle$. We find that $C_j(nT)$ does not attain its ETH predicted value at $\omega_D = \omega_m^*$ beyond a critical V_1 ; instead it saturates to a finite value, larger than a lower bound that can be obtained using Mazur's inequality^{29,30,39,40}, as expected in a system with strong HSF²⁸. In contrast, for $\omega_D \neq \omega_m^*$, C_j obeys ETH. Fourth, we study the equal-time correlation function

$$\chi_j(nT) = \langle \psi_f(nT) | \hat{n}_j \hat{n}_{j+2} | \psi_f(nT) \rangle \quad (3)$$

of Fermions starting from frozen states (Fock states $|\psi_f\rangle$ which are eigenstates of $H_F^{(1)}$). The dynamics of these states, at $\omega_D = \omega_m^*$, arise solely due to presence of higher order terms in the Floquet Hamiltonian; consequently, for large V_1 , $\chi(nT)$ remain close to their initial values at $\omega_D = \omega_m^*$ over a large range of n for random frozen initial states. In contrast, they saturate to the ETH predicted value at other frequencies. Moreover, for the frozen state $|\psi_f\rangle = |Z_2\rangle \equiv |0, 1, 0, 1, \dots\rangle$, we find the existence of novel oscillatory dynamics of $\chi_j(nT)$ when $J/V_0 \ll 1$; we provide a semi-analytic explanation of this dynamics and tie the existence of such oscillations to both the broken Z_2 symmetry of the initial Fock state and the presence of HSF which confines the dynamics to a small class of states in the Hilbert space.

FPT and Floquet Hamiltonian: To derive the Floquet Hamiltonian for the driven chain, we start from Eq. 1 and adapt a perturbative scheme (FPT) where J/V_1 is the small parameter; this distinguishes it from standard high-frequency Magnus expansion^{41–43}. Within this scheme, one computes the evolution operator corresponding to $H_0(t)$ exactly; $U_0(t, 0) = \mathcal{T} \exp[-i \int_0^t dt' H_0(t')/\hbar]$, where \mathcal{T} is the time ordering operator. The contribution of H_1 to the full evolution operator $U(t, 0)$ is then computed using standard perturbation theory. To first order in perturbation, this leads to $U_1(T, 0) = (-i/\hbar) \int_0^T dt (U_0(t, 0))^\dagger H_1 U_0(t, 0)$ and yields the leading order Floquet Hamiltonian $H_F^{(1)} = i\hbar U_1(T, 0)/T$. A straightforward calculation detailed in Ref. 40 leads to

$$H_F^{(1)} = \sum_{j=1..L} \hat{n}_j (V_0 \hat{n}_{j+1} + V_2 \hat{n}_{j+2}) - J \sum_{j=1..L} [(1 - \hat{A}_j^2) + f(\gamma_0) \hat{A}_j^2] c_j^\dagger c_{j+1} + \text{h.c.} \quad (4)$$

where $\hat{A}_j = (\hat{n}_{j+2} - \hat{n}_{j-1})$, $\gamma_0 = V_1 T/(4\hbar)$ and $f(\gamma_0) = J_0[2\gamma_0/\pi]$ for the cosine protocol and $f(\gamma_0) = \gamma_0^{-1} \sin \gamma_0 \exp[i\gamma_0 \hat{A}_j]$ for the square-pulse protocol, where J_0 is the zeroth order Bessel function.

Eq. 4 represents the central result of this work; it shows the existence of special drive frequencies $\omega_D = \omega_m^*$ for which $f(\gamma_0) = 0$. These correspond to $\gamma_0 = \pi \zeta_m/2$ and $\gamma_0 = m\pi$ respectively for the cosine and square-pulse

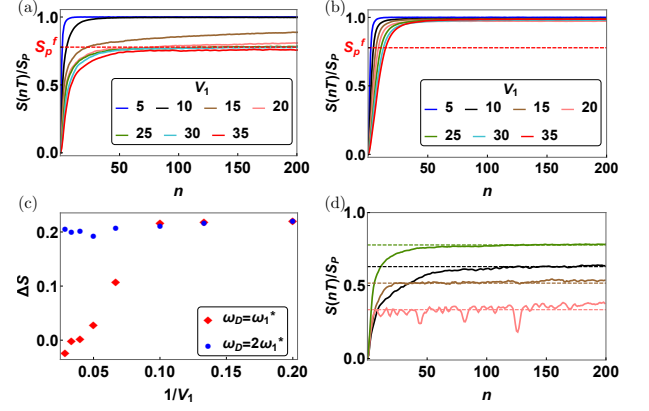


FIG. 1: (a) Plot of $S(nT)/S_p$ as a function of n for ω_1^* and several V_1 starting from a random Fock state. The red dotted line corresponds to S_p^f/S_p of the largest fragment of $H_F^{(1)}$ with HSD 1008 to which the initial state belongs. $S(nT)$ saturates to $S_p^f = 0.8S_p$ for large V_1 and $n \leq 200$. (b) Same as (a) but at $2\omega_1^*$; here S saturates to S_p for all V_1 . (c) Plot of $\Delta S = (S(nT) - S_p^f)/S_p$ as a function of $1/V_1$ for $n = 200$. $\Delta S \rightarrow 0$ at ω_1^* and for large V_1 . (d) Plot of $S(nT)/S_p$ for $V_1 = 25$ and at ω_1^* corresponding to several initial Fock states belonging to fragments of $H_F^{(1)}$ with HSD 1008 (green), 288 (black), 144 (brown) and 56 (pink). The dotted lines correspond to S_p^f/S_p to which $S(nT)/S_p$ saturates for $n \leq 200$. All plots indicate clear signature of prethermal strong HSF at ω_1^* . For all plots $L = 16$, $V_0 = V_2 = 2$ and all energies are scaled in units of J .

protocols, where m is a positive integer and ζ_m denotes the position of the m^{th} zero of J_0 . This yields

$$\begin{aligned} \omega_m^* &= V_1/(\hbar \zeta_m) \quad \text{for cosine protocol} \\ &= V_1/(2\hbar m) \quad \text{for square - pulse protocol} \end{aligned} \quad (5)$$

At these frequencies, $H_F^{(1)}$ reduces to the constrained hopping Hamiltonian studied in Refs. 32,33 which is known to show strong HSF. Such constrained Hamiltonian hosts several conserved quantities, namely, the Fermion density $N = \sum_j \hat{n}_j/L$, $N_d = \sum_j \hat{n}_j \hat{n}_{j+1}$, and $N'_d = \sum_j (-1)^j \hat{n}_j \hat{n}_{j+1}$; the corresponding Hilbert space splits into exponentially large number of fragments including exponentially large number of frozen states $|\psi_f\rangle$. Furthermore, in the high-drive amplitude regime, a straightforward calculation detailed in Ref. 40 shows that the higher order terms of H_F are suppressed by at least a factor of J/V_1 . Thus in this regime, we expect the driven Fermion chain to show signatures of HSF in the prethermal regime at $\omega_D = \omega_m^*$. For the rest of this work, we present our numerical results using the square-pulse protocol; the corresponding results for the cosine drive protocol is presented in Ref. 40.

Entanglement entropy: To find signature of fragmentation in the driven chain, we first study $S(nT)$ starting from a random Fock state $|\psi_0\rangle$ as a function of the number of drive cycles n . To this end, we numerically compute $U(T, 0)$ using ED; the details of the pro-

cedure is outlined in Ref. 40. This allows us to obtain $|\psi(nT)\rangle = U(nT, 0)|\psi_0\rangle$. One then constructs the density matrix $\rho(nT) = |\psi(nT)\rangle\langle\psi(nT)|$ for the driven chain. Finally one carries out a partial trace of $\rho(nT)$ over half the chain, to obtain the reduced density matrix $\rho_{\text{red}}(nT)$ ¹⁷; this leads to $S(nT) = -\text{Tr}[\rho_{\text{red}}(nT) \ln \rho_{\text{red}}(nT)]$.

For an ergodic chain, one expects $S(nT)$ to saturate to the symmetry resolved Page value S_p ³⁸ corresponding to the symmetry sector to which the initial state belongs. In contrast, for a system with HSF, it saturates to the Page value S_p^f of the fragment of $H_F^{(1)}$ to which the initial state belongs; since for strong HSF the Hilbert space dimension (HSD) of any fragment is exponentially smaller than the total HSD, $S_p^f < S_p$.

In Fig. 1, plots of $S(nT)$ corresponding to the symmetry sector $N = \sum_j n_j/L = 1/2$ are shown. For these plots we have chosen $V_0 = V_2 = 2J$ and used periodic boundary condition. Fig. 1(a) shows that for $\omega_D = \omega_1^*$ and large V_1/J , $S(nT)$ saturates to $S_p^f \simeq 0.8S_p$ till $n \sim 200$. In contrast, it saturates to S_p for small V_1/J . We find a clear crossover between these two regimes. This behavior is to be contrasted with its counterpart at $2\omega_1^*$ (Fig. 1(b)), where $S(nT)$ always saturates to S_p within $n \leq 50$. The dependence of $\Delta S = (S(nT) - S_p^f)/S_p$ on $1/V_1$ for both ω_1^* (red dots) and $2\omega_1^*$ (blue dots) for $n = 200$ is shown in Fig. 1(c). The latter always stays finite indicating proximity to S_p while the former sharply drops to zero beyond a critical drive amplitude. Finally, we compute $S(nT)/S_p$ for several random Fock states which belong to different Hilbert space fragments of $H_F^{(1)}$. We find that for $V_1/J = 25$ and at ω_1^* , $S(nT)$ for these initial states saturate to their respective S_p^f . All these features show a clear signature of prethermal HSF at ω_1^* .

Autocorrelation: For further signature of HSF at large V_1 , we study the autocorrelation function $C_{j=L}(nT) \equiv C_L(nT)$ (Eq. 2) using ED as a function of n . For this purpose, we use open boundary condition and set $V_0 = V_2 = 2J$. It is well-known that the presence of HSF leads to a finite long-term value of the autocorrelator which is bounded from below^{29,30,39,40}; for the present system, this bound is estimated to be 0.125⁴⁰. In contrast it decays to its ETH predicted value, $C_{\text{ETH}} = 0$, in the absence of HSF. The behavior of $C_j(nT)$ for $j \neq L$ is qualitatively similar^{30,40}.

The results for $C_L(nT)$ are shown in Fig. 2. Fig. 2(a) shows the behavior of $C_L(nT)$ as a function of n at ω_1^* for several V_1/J . We again find that for large V_1/J , $C_L(nT)$ stays above the lower bound 0.125 and close to its value predicted by $H_F^{(1)}$ exhibiting strong HSF for a large number of drive cycles. The behavior of $C_L(nT)$ for other drive frequencies are shown in Fig. 2(b) for $V_1 = 25J$; the plot clearly indicates that deviation from ω_1^* leads to rapid, ETH predicted, thermalization of $C_L(nT)$.

The plot of $C_L(nT)$ for $n = 5000$ at ω_1^* is shown as a function of V_1/J in Fig. 2(c) for several system sizes (L). We find C_L becomes almost independent of L at both large and small V_1/J ; in between, the crossover region

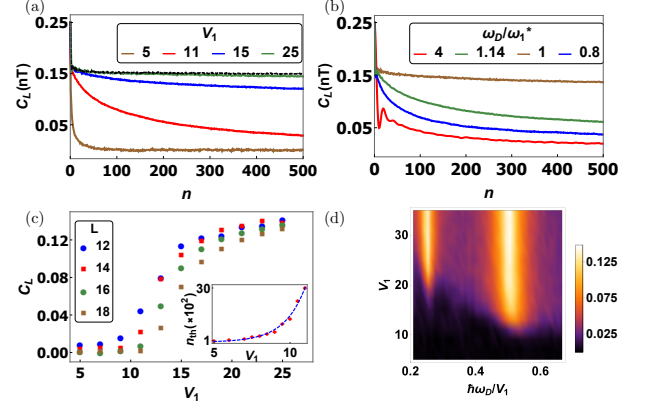


FIG. 2: (a) $C_L(nT)$ as a function of n at ω_1^* computed using exact H_F for several V_1 starting from a random thermal state. For large V_1 , $C_L(nT)$ saturates to the black dotted line which corresponds to its value computed using $H_F^{(1)}$ indicating prethermal HSF. (b) Plot of $C_L(nT)$ as a function of n for several ω_D for $V_1 = 19$ showing ETH predicted thermalization away from ω_1^* . (c) Plot of $C_L(nT)$ for $n = 5000$ as a function of V_1 at ω_1^* for several L showing a clear crossover to a prethermal HSF regime at large V_1 . The inset shows the number of cycles, n_{th} , required for $C_L(nT)$ to reach its ETH predicted value at ω_1^* for $L = 16$; n_{th} scales exponentially with V_1 showing a long prethermal regime at large V_1 . (d) Phase diagram obtained from plot of $C_L(nT)$ for $n = 5000$ as a function of V_1 and $\hbar\omega_D/V_1$ showing clear signature of finite value of C_L at large V_1 at $\hbar\omega_{1(2)}^* = V_1/(2(4))$. For all plots $V_0 = V_2 = 2$ and all energies are scaled in units of J . $L = 16$ for (a) and (b) and $L = 14$ for (d).

reduces in width with increasing L . This may indicate a sharp transition in the thermodynamic limit; however, it is difficult to conclude this from the present data.

The inset of Fig. 2(c), shows a plot of n_{th} , the number of drive cycles required for C_L to reach the ETH predicted value, as a function of V_1/J . The data clearly demonstrates exponential scaling of n_{th} with V_1/J ^{7,44,45}. A numerical fit suggests $n_{\text{th}} \sim \exp[0.72V_1/J]$. This behavior of n_{th} can be understood as follows. It is expected that for large ω_D , the extent of the prethermal regime scales exponentially with ω_D : $n_{\text{th}} \sim \exp[c_0 \hbar\omega_D/J]$ where c_0 is a constant⁴⁴. In the present case, $\omega_D = \omega_1^*$; so one expects $n_{\text{th}} = \exp[c_0 V_1/(2J)]$ which yields the exponential scaling. The numerical value of c_0 is determined to be order unity from our numerics; an analytic estimate of c_0 , which necessitates information about breakdown of convergence of the FPT series, is beyond the scope of the present work. However, we would like to point out that this exponential scaling indicates a long and stable prethermal regime where HSF signatures can be found.

Finally, in Fig. 2(d), we show a phase diagram distinguishing between regimes displaying ETH predicted thermal and HSF features of C_L as a function of V_1/J and $\hbar\omega_D/V_1$. The plot represents a clear crossover between the two regimes at both $\omega_1^* = V_1/(2\hbar)$ and $\omega_2^* = V_1/(4\hbar)$ as V_1/J is increased; we note that this is consistent with

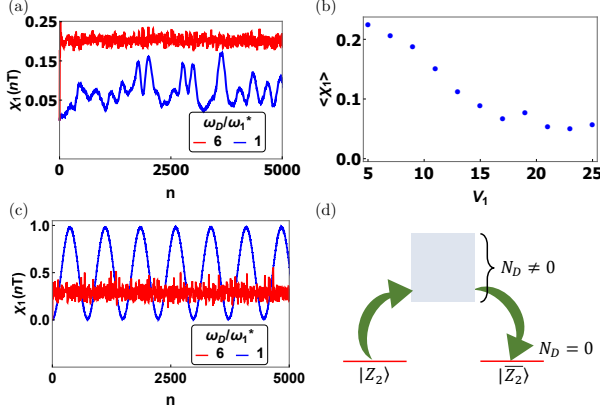


FIG. 3: (a) Plot of $\chi_1(nT)$ as a function of n for $V_1 = 19$ at ω_1^* (blue curve) and $6\omega_1^*$ (red curve) starting from a random frozen state showing lack of ETH predicted thermalization at ω_1^* . (b) Plot of $\langle\chi_1\rangle$ as a function of V_1 at ω_1^* ; $\langle\chi_1\rangle$ stays close to its initial value for large V_1 which is consistent with prethermal HSF. (c) Same as in (a) but for initial $|Z_2\rangle$ state showing slow oscillations at ω_1^* . (d) Schematic diagram for the Floquet quasienergies showing doubly degenerate $|Z_2\rangle$ and $|\bar{Z}_2\rangle$ with $N_d = 0$ and other states with $N_d \neq 0$. The arrows indicate transition to $|\bar{Z}_2\rangle$ from $|Z_2\rangle$ using intermediate states with $N_d \neq 0$ leading to slow oscillations. For all plots $V_0 = 10V_2 = 2$, $L = 14$, and all energies are scaled in units of J .

our theoretical expectation based on $H_F^{(1)}$.

Dynamics of frozen states: The frozen states correspond to Fock states which are eigenstates of $H_F^{(1)}$; however, they have non-trivial evolution under H_F due to higher order terms in FPT. The nature of this evolution, for a random frozen state with no particular symmetries, is expected to obey ETH away from ω_m^* ; in contrast, at ω_m^* , they are expected to stay close to their initial values at large drive amplitudes for a wide range of n .

To capture this behavior we plot $\chi_{j=1}(nT) \equiv \chi_1(nT)$ (Eq. 3) as a function of n in Fig. 3(a) for ω_1^* and $6\omega_1^*$ at $V_1 = 19J$. These computations are done for chains with periodic boundary conditions and $V_0 = 10V_2 = 2J$. The plot clearly shows that $\chi_1(nT)$ reaches its ETH predicted value for $6\omega_1^*$; in contrast it never reaches the ETH predicted value at ω_1^* . The plot of $\langle\chi_1\rangle$ ($\chi_1(nT)$ averaged over 5000 drive cycles starting from $n = 5000$) as a function of V_1/J at ω_1^* is shown in Fig. 3(b). We find that $\langle\chi_1\rangle$ stays close to its initial value at large V_1/J which is consistent with prethermal strong HSF. We have checked that this behavior is similar for all $\langle\chi_j\rangle$.

Next we study the dynamics of frozen state when $|\psi_f\rangle = |Z_2\rangle$. As shown in Fig. 3(c), when the system is driven at ω_1^* (blue curve), the equal-time correlation function $\chi_1(nT)$ shows slow oscillations with a time period that is orders of magnitude longer than the bare time scales implied in the Hamiltonian of Eq. (1). On the other hand, the oscillations are absent for $6\omega_1^*$ (red curve in Fig. 3(c)). In fact, the occurrence of the slow oscillations require two conditions to be satisfied. First, the system

has to be fragmented in a prethermal sense so that, starting from the state $|Z_2\rangle$, over long time scales the system stays effectively confined in the $N_D = 0$ sector with no nearest neighbor occupations. This sector comprises the states $|Z_2\rangle$ and $|\bar{Z}_2\rangle \equiv |1, 0, 1, 0, \dots\rangle$. Second, the energy scales $J/V_0 \lesssim 1$ and $V_2/V_0 \leq 1/2$, so that $N_D = 0$ is the lowest energy manifold in the Fock space, while $N_D \neq 0$ are high energy states as shown in Fig. 3(d). In such a situation the higher order terms in FPT provide tunneling paths for the system to oscillate between $|Z_2\rangle$ and $|\bar{Z}_2\rangle$. Since $\hat{n}_1\hat{n}_3|Z_2\rangle = 0$, while $\hat{n}_1\hat{n}_3|\bar{Z}_2\rangle = 1$, the equal-time correlation function $\chi_1(nT)$ oscillates between zero and nearly one (the deviation from one is due to finite mixing with the states in the $N_D \neq 0$ sectors). In other words, the oscillations are manifestation of the tunneling processes that restore Z_2 symmetry in a finite system such that the approximate eigenstates of H_F are the bonding and antibonding states $|\psi_{B,A}\rangle \equiv |Z_2\rangle \pm |\bar{Z}_2\rangle$. Therefore, the oscillation frequency is proportional to the energy split $2\hbar\alpha_d$ between the bonding and antibonding states; this is expected to be a small energy scale as it arises from higher order terms in H_F (which we verified using ED). Thus, if $H_F|\psi_{B,A}\rangle \approx \hbar(\alpha_s \pm \alpha_d)|\psi_{B,A}\rangle$ for a constant α_s , one can show that $\chi_1(nT) \approx \sin^2(\alpha_d nT)$ which explains the slow oscillations. In passing we note that similar oscillations also appear in the fidelity function $F(nT) \equiv |\langle Z_2(0)|Z_2(nT)\rangle|^2$ [40].

Discussion: In conclusion, we have shown that a driven Fermion chain, in the high drive amplitude regime, exhibits signature of strong HSF in the prethermal regime at special drive frequencies. This constitutes the first realization of strong HSF in out-of-equilibrium systems. We have provided analytic expressions for these special frequencies and have supported this claim by exact numerical computation of entanglement entropy, autocorrelation and equal-time correlation function of the Fermions. We have also studied the dynamics of these Fermions starting from frozen states and have identified a novel oscillatory dynamics for the $|Z_2\rangle$ initial state; such oscillations arise due to both HSF and Z_2 symmetry breaking. We expect our results to be of relevance for ultracold atom platforms where such Fermion chains may be experimentally realized^{34,46}.

Appendix A: Floquet Perturbation Theory

In this section, we provide the details of the Floquet perturbation theory computations outlined in the text for both the cosine and the square-pulse protocols. To this end, we first note that in the large drive amplitude limit, where $V_1 \gg V_0, J, V_2$, one can write the Hamilto-

nian $H(t) = H_0(t) + H_1$, where

$$\begin{aligned} H_0(t) &= V(t) \sum_j \hat{n}_j \hat{n}_{j+1} \\ H_1 &= -J \sum_j (c_j^\dagger c_{j+1} + \text{h.c.}) + V_0 \sum_j \hat{n}_j \hat{n}_{j+1} \\ &\quad + V_2 \sum_j \hat{n}_j \hat{n}_{j+2} \end{aligned} \quad (\text{A1})$$

where $V(t) = V_1 f(t)$ and $f(t)$ is a periodic function with time period T . The precise form of $f(t)$ depends on the protocol as outlined in the main text; for the cosine-drive protocol, $f(t) = \cos \omega_D t$, where $\omega_D = 2\pi/T$ is the drive frequency while for the square-pulse protocol $f(t) = -1(1)$ for $t \leq (>)T/2$.

Starting from Eq. A1, we first construct the evolution operator

$$U_0(t, 0) = \mathcal{T} \left[e^{-i \int_0^t dt' H_0(t')/\hbar} \right] \quad (\text{A2})$$

Using Eq. A1, this can be evaluated to obtain

$$U_0^c(t, 0) = e^{-iV_1 \sin \omega_D t \sum_j \hat{n}_j \hat{n}_{j+1}/(\hbar \omega_D)} \quad (\text{A3})$$

for the cosine drive protocol and

$$\begin{aligned} U_0^s(t, 0) &= e^{iV_1 t \sum_j \hat{n}_j \hat{n}_{j+1}/\hbar}, \quad t \leq T/2 \\ &= e^{iV_1 (T-t) \sum_j \hat{n}_j \hat{n}_{j+1}/\hbar}, \quad t > T/2 \end{aligned} \quad (\text{A4})$$

for the square-pulse protocol. Note that for both protocols $U_0^c(T, 0) = U_0^s(T, 0) = I$, where I denotes the identity matrix; this leads to $H_F^{(0)} = 0$ for both protocols.

To obtain the first order Floquet Hamiltonian, we now treat H_1 perturbatively following Refs. 18,41. First, we consider the continuous protocol for which the first order correction to U_0^c is given by

$$U_1^c(T, 0) = \frac{-i}{\hbar} \int_0^T dt (U_0^c(t, 0))^\dagger H_1 U_0^c(t, 0) \quad (\text{A5})$$

To evaluate U_1^c , we note that the terms in H_1 involving V_0 and V_2 (Eq. A1) commute with H_0 and hence with U_0^c while the hopping term does not. To understand the effect of the hopping term, we consider the action of U_0^c on an arbitrary Fock state $|m\rangle$. Since $H_0(t)$ is diagonal in the Fock basis, one can write

$$\begin{aligned} U_0^c(t, 0)|m\rangle &= e^{-iE_m \sin \omega_D t/(\hbar \omega_D)}|m\rangle \equiv e^{-i\theta_m}|m\rangle, \\ V_1 \sum_j \hat{n}_j \hat{n}_{j+1}|m\rangle &= E_m|m\rangle. \end{aligned} \quad (\text{A6})$$

Now let us consider the action of the hopping term in H_1 on the state $|m\rangle$: $-Jc_j^\dagger c_{j+1}|m\rangle = |n\rangle$. We note that $|m\rangle$ and $|n\rangle$ have different occupation numbers only on the j^{th} and $(j+1)^{\text{th}}$ sites. It is then easy to see that

$$\begin{aligned} E_m &= E_n, \quad \text{if } A_j|m\rangle = 0 \\ &= E_n \pm V_1, \quad \text{if } A_j|m\rangle = \pm|m\rangle \\ A_j &= (\hat{n}_{j+2} - \hat{n}_{j-1}) \end{aligned} \quad (\text{A7})$$

The result of Eq. A7 can be understood in the following manner. We find that the phase θ_m of any Fock state can change due to local hopping if this process changes the number of nearest neighbor pairs; such a change can only occur if A_j is non-zero. Using this, one can carry out the computation of U_1^c following standard methods outlined in Ref. 18,41. This yields

$$\begin{aligned} U_1^c(T, 0) &= \frac{-iT}{\hbar} \sum_j \hat{n}_j (V_0 \hat{n}_{j+1} + V_2 \hat{n}_{j+2}) \\ &\quad + \frac{iTJ}{\hbar} \sum_j \left[J_0 \left(\frac{2\gamma_0 A_j}{\pi} \right) c_j^\dagger c_{j+1} + \text{h.c.} \right] \end{aligned} \quad (\text{A8})$$

where $\gamma_0 = V_1 T/(4\hbar)$, J_0 denotes the zeroth order Bessel function and we have used the identity $\exp[i\alpha \sin x] = \sum_m J_m(\alpha) \exp[imx]$. Next using the properties $J_0(x) = J_0(-x)$ and $J_0(0) = 1$ and noting that A_j can only have values $0, \pm 1$ for any j , we write

$$J_0 \left(\frac{2\gamma_0 A_j}{\pi} \right) = J_0 \left(\frac{2\gamma_0}{\pi} \right) A_j^2 + (1 - A_j^2) \quad (\text{A9})$$

This allows us to write

$$\begin{aligned} U_1^c(T, 0) &= \frac{-iT}{\hbar} \sum_j \hat{n}_j (V_0 \hat{n}_{j+1} + V_2 \hat{n}_{j+2}) \\ &\quad + \frac{iTJ}{\hbar} \sum_j \left[\left(J_0 \left(\frac{2\gamma_0}{\pi} \right) A_j^2 + (1 - A_j^2) \right) c_j^\dagger c_{j+1} + \text{h.c.} \right] \end{aligned} \quad (\text{A10})$$

This leads to $H_F^{(1,c)} = i\hbar U_1(T, 0)/T$ which is given by

$$\begin{aligned} H_F^{(1,c)} &= \sum_j \hat{n}_j (V_0 \hat{n}_{j+1} + V_2 \hat{n}_{j+2}) \\ &\quad - J \sum_j \left[\left(J_0 \left(\frac{2\gamma_0}{\pi} \right) A_j^2 + (1 - A_j^2) \right) c_j^\dagger c_{j+1} + \text{h.c.} \right] \end{aligned} \quad (\text{A11})$$

which is the result used in the main text.

Next, we consider the second order term. To second order, the evolution operator is given by

$$\begin{aligned} U_2^c(T, 0) &= \left(\frac{-i}{\hbar} \right)^2 \int_0^T dt_1 U_0^{c\dagger}(t_1, 0) H_1 U_0^c(t_1, 0) \\ &\quad \times \int_0^{t_1} dt_2 U_0^{c\dagger}(t_2, 0) H_1 U_0^c(t_2, 0). \end{aligned} \quad (\text{A12})$$

The second order contribution to the Floquet Hamiltonian is given, in terms of U_2^c by

$$H_F^{(2,c)}(T, 0) = \frac{i\hbar}{T} (U_2^c(T, 0) - [U_1^c(T, 0)]^2/2) \quad (\text{A13})$$

From Eqs. A13 and A12, it is easy to see that there is no contribution to $H_F^{(2,c)}$ from terms in H_1 which commutes with U_0^c ; their contributions to U_2^c and $(U_1^c)^2/2$ cancel each other. Thus the only contribution to $H_F^{(2)}$

comes from the hopping term. A straightforward, albeit somewhat lengthy, calculation yields

$$\begin{aligned}
H_F^{(2,c)}(T, 0) &= -\frac{2J^2}{\hbar\omega_D} C_0 \left(\frac{2\gamma_0}{\pi} \right) \sum_{j_1, j_2} [O_{j_1}^{(1)}, O_{j_2}^{(2)}] \\
C_0(\alpha) &= \sum_{m=0}^{\infty} J_{2m+1}(\alpha)/(2m+1) \\
O_{j_1}^{(1)} &= \left[\left(J_0 \left(\frac{2\gamma_0}{\pi} \right) A_{j_1}^2 + (1 - A_{j_1}^2) \right) \right. \\
&\quad \left. \times c_{j_1}^\dagger c_{j_1+1} + \text{h.c.} \right] \\
O_{j_2}^{(2)} &= A_{j_2} c_{j_2+1}^\dagger c_{j_2} - \text{h.c.} \quad (\text{A14})
\end{aligned}$$

where we have used the fact that $J_{2m+1}(-x) = -J_{2m+1}(x)$ and $J_{2m+1}(0) = 0$. The commutator structure of $H_F^{(2,c)}$ ensures that it is local. Furthermore, $\|H_F^{(2,c)}\| < \|H_F^{(1,c)}\|$ for $J/(\hbar\omega_D) < 1$; this ensures that one can use this perturbative scheme in the intermediate frequency regime, where $\hbar\omega_D < V_1$. However, we note that the above-mentioned criteria does not ensure that the perturbation series shall converge for $\hbar\omega_D \sim J$; estimating the radius of convergence of such an expansion is beyond the scope of the present work.

Next we consider the square pulse protocol. For this the first order Floquet Hamiltonian can be written as

$$U_1^s(T, 0) = \frac{-i}{\hbar} \left(\int_0^{T/2} dt e^{-iV_1 t \sum_j \hat{n}_j \hat{n}_{j+1}/\hbar} H_1 e^{iV_1 t \sum_j \hat{n}_j \hat{n}_{j+1}/\hbar} + \int_{T/2}^T e^{-iV_1 (T-t) \sum_j \hat{n}_j \hat{n}_{j+1}/\hbar} H_1 e^{iV_1 (T-t) \sum_j \hat{n}_j \hat{n}_{j+1}/\hbar} \right) \quad (\text{A15})$$

Eq. A15 can be evaluated exactly as done for the continuous protocol. We define the phase θ'_m via the relation $U_0^s(t, 0)|m\rangle = \exp[i\theta'_m]|m\rangle$ and then note that the action of a local hopping term can change this phase only if it changes the number of nearest neighbor pairs. This condition can again be implemented using the operator A_j . This leads to

$$\begin{aligned}
U_1^s(T, 0) &= \frac{-iT}{\hbar} \sum_j \hat{n}_j (V_0 \hat{n}_{j+1} + V_2 \hat{n}_{j+2}) \quad (\text{A16}) \\
&+ \frac{iTJ}{\hbar} \sum_j \frac{\sin \gamma_0 A_j}{\gamma_0 A_j} e^{i\gamma_0 A_j} c_j^\dagger c_{j+1} + \text{h.c}
\end{aligned}$$

Noting that $A_j = 0, \pm 1$, one can then write

$$\frac{\sin \gamma_0 A_j}{\gamma_0 A_j} e^{i\gamma_0 A_j} = \frac{\sin \gamma_0}{\gamma_0} A_j^2 e^{i\gamma_0 A_j} + (1 - A_j^2) \quad (\text{A17})$$

Using Eq. A17 and the relation $H_F^{(1,s)} = i\hbar U_1^s(T, 0)/T$, one finally gets

$$H_F^{(1,s)}(T, 0) = \sum_j \hat{n}_j (V_0 \hat{n}_{j+1} + V_2 \hat{n}_{j+2}) - J \sum_j \left(\left[\frac{\sin \gamma_0}{\gamma_0} e^{i\gamma_0 A_j} A_j^2 + (1 - A_j^2) \right] c_j^\dagger c_{j+1} + \text{h.c} \right) \quad (\text{A18})$$

which yields the result of the main text.

The second order contribution to $H_F^{(2)}$ for the square-pulse protocol vanishes. This can be seen as follows. The second order evolution operator for the square pulse protocol is given analogously by

$$\begin{aligned}
U_2^s(T, 0) &= \left(\frac{-i}{\hbar} \right)^2 \int_0^T dt_1 U_0^{s\dagger}(t_1, 0) H_1 U_0^s(t_1, 0) \\
&\times \int_0^{t_1} dt_2 U_0^{s\dagger}(t_2, 0) H_1 U_0^s(t_2, 0). \quad (\text{A19})
\end{aligned}$$

and the corresponding second order Floquet Hamiltonian reads

$$H_F^{(2,s)}(T, 0) = \frac{i\hbar}{T} (U_2^s(T, 0) - [U_1^s(T, 0)]^2/2) \quad (\text{A20})$$

Using the form of the zeroth order evolution operator from Eq. A4, it can be easily shown that the integral in Eq. A19 can be split into three non-zero integrals of the general form

$$\begin{aligned}
I_1 &= \int_0^T dt_1 \int_0^{t_1} dt_2 \theta(T/2 - t_1) \theta(T/2 - t_2) f(t_1) g(t_2) \\
I_2 &= \int_0^T dt_1 \int_0^{t_1} dt_2 \theta(t_1 - T/2) \theta(t_2 - T/2) f(T - t_1) g(T - t_2) \\
I_3 &= \int_0^T dt_1 \int_0^{t_1} dt_2 \theta(t_1 - T/2) \theta(T/2 - t_2) f(T - t_1) g(t_2)
\end{aligned} \tag{A21}$$

with $\theta(t)$ being the Heaviside step function and $f(t)$, $g(t)$ being well-behaved functions of t , whose exact form depends on the details of H_1 and $U_0^s(t, 0)$.

By shifting the limits of these integrals appropriately, one can show that

$$I_1 + I_2 + I_3 = 2 \int_0^{T/2} d\tau_1 f(\tau_1) \int_0^{T/2} d\tau_2 g(\tau_2), \tag{A22}$$

thus implying that the second order evolution operator

$$\begin{aligned}
U_2^s(T, 0) &= 2 \left(\frac{-i}{\hbar} \right)^2 \int_0^{T/2} dt_1 U_0^{s\dagger}(t_1, 0) H_1 U_0^s(t_1, 0) \\
&\quad \times \int_0^{T/2} dt_2 U_0^{s\dagger}(t_2, 0) H_1 U_0^s(t_2, 0). \tag{A23}
\end{aligned}$$

Using the same logic, the first order evolution operator in Eq. A15 has the form $U_1^s(T, 0) = 2 \left(\frac{-i}{\hbar} \right) \int_0^{T/2} dt_1 U_0^{s\dagger}(t_1, 0) H_1 U_0^s(t_1, 0)$, so that

$$U_2^s(T, 0) = \frac{[U_1^s(T, 0)]^2}{2} \tag{A24}$$

which implies from Eq. A20 that $H_F^{(2,s)}(T, 0) = 0$. Thus the leading order correction to $H_F^{(1)}$ for the square-pulse protocol comes from the third-order terms which are $\sim J^3/V_1^2$; we do not aim to compute them in this work.

Appendix B: Half-Chain Entanglement Entropy Computation and Calculation of Page Value

In this section, we outline the procedure for the numerical computation of the half-chain entanglement entropy and analytical calculation of Page value used in Fig. 1 of the main text. This procedure is applicable for any arbitrary pure state drawn from the Hilbert space.

We divide the chain into two halves, A and B , such that the full Hilbert space of the system can be represented as $\mathcal{H} = \mathcal{H}_A \otimes \mathcal{H}_B$. In the computational basis, any arbitrary state of the whole chain can be written as

$$|\psi\rangle = \sum_{i,j} c_{i,j} |i_A\rangle \otimes |j_B\rangle \tag{B1}$$

where $c_{i,j}$, which are elements of a matrix C , are, in general, complex numbers and $\{|i_A\rangle\}$ and $\{|j_B\rangle\}$ span \mathcal{H}_A and \mathcal{H}_B respectively.

Next, using singular value decomposition (also known as Schmidt decomposition in this particular case), we obtain the matrix \tilde{C} such that $C = P\tilde{C}Q^\dagger$. Here P and Q are unitary matrices and \tilde{C} is a diagonal matrix with real, non-negative entries \tilde{c}_{kk} . Substituting this in Eq. B1 we find

$$\begin{aligned}
|\psi\rangle &= \sum_{i,j,k} p_{ik} \tilde{c}_{kk} q_{jk}^* |i_A\rangle \otimes |j_B\rangle \\
&= \sum_k \tilde{c}_{kk} |k_A\rangle \otimes |k_B\rangle
\end{aligned} \tag{B2}$$

where $|k_A\rangle = \sum_i p_{ik} |i_A\rangle$ and $|k_B\rangle = \sum_j q_{jk}^* |j_B\rangle$ are the transformed basis vectors with unitary matrices P^T and Q^\dagger respectively.

The density matrix of the full system in this basis reads

$$\rho = |\psi\rangle\langle\psi| = \sum_{k,k'} \tilde{c}_{kk} \tilde{c}_{k'k'} (|k_A\rangle\langle k_B|)(\langle k'_B|\langle k'_A|). \tag{B3}$$

In order to obtain the reduced density matrix corresponding to one of the halves, we trace over the degrees of freedom of the other half. Without loss of generality, we choose to trace out the degrees of freedom in B . This yields

$$\begin{aligned}
\rho_A &= \text{Tr}_B \rho \\
&= \sum_k \tilde{c}_{kk}^2 |k_A\rangle\langle k_A|
\end{aligned} \tag{B4}$$

The half-chain entanglement entropy S_A is then given by $S_A = -\text{Tr}_A \rho_A \ln \rho_A$. Since the reduced density matrix, ρ_A is diagonal in this basis, its eigenvalues can be easily read off as \tilde{c}_{kk}^2 , which implies that

$$S_A = - \sum_k \tilde{c}_{kk}^2 \ln \tilde{c}_{kk}^2 \tag{B5}$$

The advantage of the Schmidt decomposition is that one can directly use \tilde{c}_{kk} (which are singular values of the coefficient matrix C) in order to evaluate the half-chain entanglement entropy numerically, without the need to compute the reduced density matrix explicitly and diagonalizing it.

To calculate the Page value of the entanglement entropy in the half-filled symmetry sector, we adopt the procedure outlined in Ref. 38. We randomly choose a

Gaussian orthogonal ensemble (GOE)-like state in this sector of the form

$$|\psi\rangle = \sum_{N_A=0}^{L/2} \sum_{b=1}^{d_B(N_B)} \sum_{a=1}^{d_A(N_A)} \frac{z_{a,b}}{\sqrt{\mathcal{D}_{L/2}}} |a; N_A\rangle |b; N_B\rangle \quad (\text{B6})$$

where $z_{a,b}$ are random real numbers chosen from a normal distribution with mean 0 and unit variance, $\mathcal{D}_{L/2}$ is the Hilbert space dimension (HSD) of the half-filled sector, and $d_A(N_A)$ and $d_B(N_B)$ are HSD's of subsystems A and B with occupancies N_A and $N_B = \frac{L}{2} - N_A$ respectively. The dimensions can be easily calculated using combinatorics as $\mathcal{D}_{L/2} = {}^L C_{L/2}$, $d_A(N_A) = {}^{L/2} C_{N_A}$ and $d_B(N_B) = {}^{L/2} C_{N_B}$.

The reduced density matrix for the subsystem A can be calculated as

$$\begin{aligned} \rho_A &= \frac{1}{\mathcal{D}_{L/2}} \sum_{N_A=0}^{L/2} \sum_{a,a'=1}^{d_A(N_A)} \mu_{aa'} |a, N_A\rangle \langle a', N_A| \\ \mu_{aa'} &= \sum_{b=1}^{d_B(N_B)} z_{a,b} z_{a',b} \end{aligned} \quad (\text{B7})$$

Averaging over the Gaussian distributed random variables and using

$$\overline{\mu_{a,a'}} = \frac{1}{d_B(N_B)} \sum_{b=1}^{d_B(N_B)} z_{a,b} z_{a',b} = d_B(N_B) \delta_{aa'}, \quad (\text{B8})$$

we get for the average reduced density matrix

$$\bar{\rho}_A = \sum_{N_A=0}^{L/2} \sum_{a=1}^{d_A(N_A)} \frac{d_B(N_B)}{\mathcal{D}_{L/2}} |a, N_A\rangle \langle a, N_A| \quad (\text{B9})$$

This implies that the mean value of the half-chain entanglement entropy (averaged over GOE states) is $\bar{S}_{L/2} = -\text{Tr}_A \rho_A \ln \rho_A$. To estimate the maximal value of $\bar{S}_{L/2}$, we use the concavity property of the function $f(x) = x \ln x$, which implies

$$\bar{S}_{L/2} \leq -\text{Tr}_A \bar{\rho}_A \ln \bar{\rho}_A = S_{L/2}^{\max} \quad (\text{B10})$$

Hence, the maximal value of the half-chain entanglement entropy for thermal GOE states is

$$S_{L/2}^{\max} = - \sum_{N_A=0}^{L/2} \frac{d_A(N_A) d_B(N_B)}{\mathcal{D}_{L/2}} \ln \frac{d_B(N_B)}{\mathcal{D}_{L/2}} \quad (\text{B11})$$

The leading correction to Eq. B11 was found to be $-\frac{1}{2}$ in Ref. 38 for the half-filled case. This is the result which we use to calculate the Page value, S_p of the entire half-filled sector in Fig. 1 of the main text. To calculate the Page value of the largest fragment, S_p^f we execute the same procedure of averaging over random canonical states from that fragment. In this case, we carry out numerical computations to obtain S_p^f .

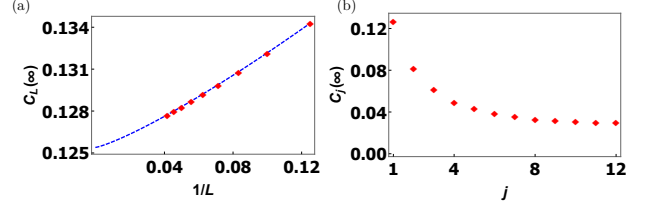


FIG. 4: (a) Scaling of the lower bound of the fermion density autocorrelator $C_L(\infty)$, obtained using $H_F^{(1)}$ with system size, L . The blue dashed line corresponds to a least square fit which predicts a lower bound close to 0.125 in the thermodynamic limit. (b) Variation of $C_j(\infty)$ with distance from one of the edges (labelled as $j = 1$) in a chain of length $L = 24$. The plot shows that the bound decreases as one moves away from the edges.

Appendix C: Lower Bound on the unequal time fermion density autocorrelation function

In this section, we establish that in the fragmented regime, the fermion density autocorrelation function, $C_L(nT)$ computed in the main text is bounded from below by a value greater than zero. This clearly implies that the system evades thermalization as the ETH predicted value of the autocorrelator is zero.

To estimate this lower bound, we consider the fragmented first order Floquet Hamiltonian, $H_F^{(1)}$, with open boundary condition and use Mazur's inequality³⁹. To this end, we define \bar{C}_j as

$$\bar{C}_j = \lim_{n \rightarrow \infty} \frac{1}{n} \sum_n \langle (\hat{n}_j(nT) - 1/2)(\hat{n}_j(0) - 1/2) \rangle \quad (\text{C1})$$

where the expectation on the RHS is taken with respect to an infinite temperature thermal state. In the presence of HSF, \bar{C}_j satisfies

$$\bar{C}_j \geq \sum_i \frac{[\text{Tr}((\hat{n}_j - 1/2)P_i)]^2}{\mathcal{D}_{L/2} \mathcal{D}_i} \equiv C_j(\infty) \quad (\text{C2})$$

where P_i is the projection operator to the i^{th} fragment and \mathcal{D}_i is its dimension, and we shall first set the coordinate $j = L$ to estimate $C_L(\infty)$. We note that the presence of higher order terms in H_F at the special drive frequencies ω_m^* will result in violation of this bound beyond the prethermal regime when $n > n_{\text{th}}$; however, as noted in the main text, in the large drive amplitude regime where the prethermal regime is long, $\bar{C}_L(nT)$ is expected to remain above $C_L(\infty)$ for a large range of $n < n_{\text{th}} \sim O(e^{V_1/J})$.

To estimate $C_L(\infty)$ using Eq. C2, we construct the matrix for $H_F^{(1)}$ in the computational basis and identify blocks of connected components. We determine the sizes of these blocks to obtain \mathcal{D}_i s and use these to evaluate $C_L(\infty)$ for a specific L . Using these values of $C_L(\infty)$ for different L , we carry out a $1/L$ extrapolation as shown in

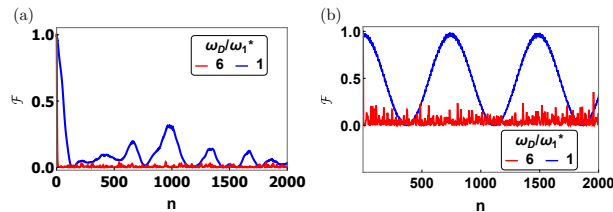


FIG. 5: (a) Evolution of fidelity \mathcal{F} starting from a random frozen state for $V_1 = 19$ and different values of the drive frequencies. \mathcal{F} remains finite for $n \leq 2000$ for $\omega_D = \omega_1^*$ (blue curve) indicating violation of ETH while it vanishes in accordance with prediction of ETH for $\omega_D = 6\omega_1^*$. (b) Same as (a) but now starting from $|Z_2\rangle$ initial state. The red curves again show thermal behavior, as expected of an ergodic system, while the blue curve exhibits persistent slow oscillation as in Fig. 3(c) of the main text. For both the figures, $V_0 = 10V_2 = 2$, $L = 14$ and all energies are scaled in units of J .

Fig. 4(a). We find that $C_L(\infty)$ attains a finite non-zero value, close to 0.125 in the thermodynamic limit, thus affirming non-thermal behavior. This is consistent with the results obtained in Fig. 2 of the main text where we find $C_L(nT) \simeq 0.15$ in the prethermal regime at $\omega_D = \omega_1^*$. We also study the variation of this lower bound with distance from one of the edges of the chain in Fig. 4(b), where we plot $C_j(\infty)$ for $L = 24$ as a function of j . We find that the bound decreases as one moves into the bulk. This behavior is consistent with that found in Refs. 29,30 and is the reason why $C_L(\infty)$ is studied in details in the main text.

Appendix D: Fidelity

In this section, we study the evolution of the fidelity $\mathcal{F} = |\langle \psi(0) | \psi(nT) \rangle|^2$ starting from a random frozen state and a $|Z_2\rangle$ state, using a square pulse protocol. We find that their behaviors are analogous to those observed for equal time local correlation functions as shown in Fig. 3 of the main text.

These results are shown in Fig. 5. Similar to the behavior of the density-density correlation function discussed in the main text, we find that for a random state \mathcal{F} does not decay to zero, as expected for an ergodic system, for $\omega_D = \omega_1^*$ (blue curve); in contrast, for $\omega_D = 6\omega_1^*$, \mathcal{F} vanishes within the first few cycles (red curve). Moreover, we find a much slower departure of \mathcal{F} from unity at ω_1^* . These features indicate a clear violation of ETH at the special frequencies.

A similar computation starting from the initial $|Z_2\rangle$ state leads to slow oscillations of \mathcal{F} for $\omega_D = \omega_1^*$ and its rapid, ETH predicted, decay at $\omega_D = 6\omega_1^*$ (red curve). The oscillations of \mathcal{F} can be explained in a similar manner as done for the correlation function χ_1 in the main text. The bonding and the antibonding states $|\psi_B\rangle = (|Z_2\rangle + |\bar{Z}_2\rangle)/\sqrt{2}$ and $|\psi_A\rangle = (|Z_2\rangle - |\bar{Z}_2\rangle)/\sqrt{2}$ form two approximate eigenstates of the exact Floquet Hamiltonian. The off-diagonal matrix elements connecting these two states receive contribution from higher order terms in H_F due to tunneling to states with $N_d \neq 0$. Following a similar argument detailed in the main text, it is easy to show that if the energy split between these two states is $2\hbar\alpha_d$, then $\mathcal{F} \sim \cos^2(\alpha_d nT)$. We note that such coherent oscillations can only happen if the system is non-ergodic and hence constitute a signature of fragmentation; however, in addition, such oscillations require Z_2 symmetry breaking of the initial state and thus does not occur for random frozen initial states.

Appendix E: Continuous drive protocol

In this section, we present results for time evolution of entanglement entropy $S(nT)$, fermion density-density autocorrelator $C_L(nT)$, and equal time density-density correlation function $\chi_1(nT)$ as a function of n for the protocol $V(t) = V_1 \cos \omega_D t$.

From the forms of $H_F^{(1,c)}$ and $H_F^{(1,s)}$ presented in Eq. A11 and A18, it is evident that the former exhibits the same structure at the special frequencies characterized by $\omega_m^* = V_1/(\hbar\zeta_m)$ as the latter at frequency $\omega_m^* = V_1/(2\hbar m)$. Here m is an integer and ζ_m is the m^{th} zero of J_0 as already outlined in the main text. Thus, we expect to witness similar signatures of prethermal fragmentation when the system is driven following a continuous drive protocol.

The plots of $S(nT)$, $C_L(nT)$ and $\chi_1(nT)$ shown in Fig. 6 confirm this expectation. The results are qualitatively similar to those obtained for square pulse protocol discussed in the main text. However, for a given drive amplitude, one witnesses more stability of HSF for the square pulse protocol as compared to its continuous counterpart. This is expected since the first non-trivial correction is third order for square pulse, whereas it is second-order for the continuous protocol. However, we note that the qualitative similarity of the plots for the two protocols indicate protocol independence for realization of prethermal strong HSF.

¹ J. M. Deutsch, Phys. Rev. A **43**, 2046 (1991); M. Srednicki, Phys. Rev. E **50**, 888 (1994); M. Srednicki, J. Phys. A **32**, 1163 (1999).

² M. Rigol, V. Dunjko, M. Olshanii, Nature **452**, 854 (2008); P. Reimann, Phys. Rev. Lett. **101**, 190403 (2008).

³ A. Polkovnikov, K., Sengupta, A. Silva, A. and M. Ven-

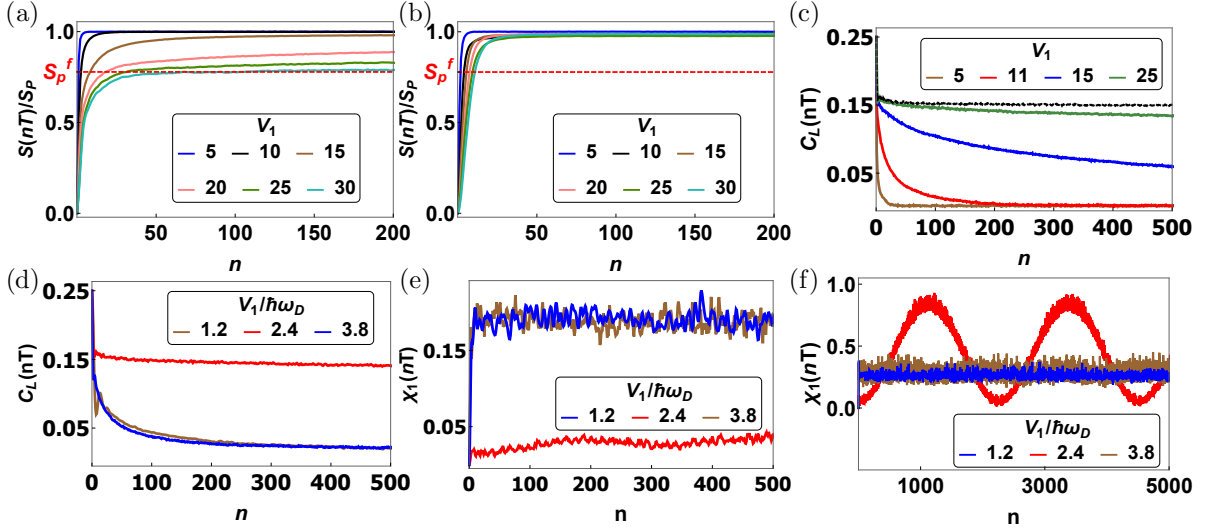


FIG. 6: (a) Evolution of entanglement entropy $S(nT)$ with drive cycle n for $V_1/(\hbar\omega_D) = \zeta_1 = 2.408$ (*i.e.* $\omega_D = \omega_1^*$) for different V_1 and starting from a random Fock state. The red dotted line corresponds to the Page value S_p^f/S_p for the largest fragment of $H_F^{(1)}$ to which the initial state belongs. (b) Same as (a) but now with $V_1/(\hbar\omega_D) = \zeta_1/2$. (c) Plot of $C_L(nT)$ as a function of n starting from a random infinite temperature thermal state for $V_1/(\hbar\omega_D) = \zeta_1$ and several V_1 . The black dashed line corresponds to the value $C_L(nT)$ attains when the evolution is carried out using $H_F^{(1)}$, while the others correspond to evolution with exact H_F . (d) Same as (c) but now with $V_1 = 30$ and different frequencies. (e) Plot of $\chi_1(nT)$ as a function of n for $V_1 = 30$ and several frequencies starting from a random frozen state. (f) Same as (e) but now starting from $|Z_2\rangle$. In (d), (e) and (f), the red curves correspond to $\omega_D = \omega_1^*$. For all the plots $V_0 = V_2 = 2$ and all energies are scaled with J .

- galattore, Rev. Mod. Phys. **83**, 863 (2011).
- ⁴ L. D'Alessio, Y. Kafri, A. Polkovnikov, and M. Rigol, Adv. Phys. **65**, 239 (2016).
 - ⁵ L. D'Alessio and M. Rigol, Phys. Rev. X **4**, 041048 (2014).
 - ⁶ M. Bukov, L. D'Alessio, and A. Polkovnikov, Adv. Phys. **64**, 139 (2014).
 - ⁷ W. W. Ho, T. Mori, D. A. Abanin, and E. G. Dalla Torre, arXiv:2212.00041 (unpublished).
 - ⁸ T. Kohlert, S. Scherg, X. Li, H. P. Luschen, S.D. Sarma, I. Bloch, and M. Aidelsburger, Phys. Rev. Lett. **122**, 170403 (2019).
 - ⁹ A. Kyprianidis, F. Machado², W. Morong¹, P. Becker¹, K. S. Collins, D. V. Else, L. Feng, P. W. Hess, C. Nayak, G. Pagano, N. Y. Yao, and C. Monroe, Science **372**, 1192 (2021).
 - ¹⁰ A. Das, Phys. Rev. B **82**, 172402 (2010); S. Bhattacharyya, A. Das, and S. Dasgupta, Phys. Rev. B **86**, 054410 (2012); S. S. Hedge, H. Katiyar, T. S. Mahesh, and A. Das, Phys. Rev. B **90**, 174407 (2014).
 - ¹¹ A. Haldar, R. Moessner, and A. Das. Phys. Rev. B **97**, 245122 (2018); A. Haldar, D. Sen, R. Moessner, and A. Das. Phys. Rev. X **11**, 021008 (2021)
 - ¹² T. Banerjee and K. Sengupta, arXiv:2209.12939 (unpublished).
 - ¹³ A. Agarwala, U. Bhattacharya, A. Dutta, and D. Sen, Phys. Rev. B **93**, 174301 (2016); A. Agarwala and D. Sen, *ibid.* **95**, 014305 (2017).
 - ¹⁴ D. J. Luitz, Y. Bar Lev, and A. Lazarides, SciPost Phys. **3**, 029 (2017); D. J. Luitz, A. Lazarides, and Y. Bar Lev, Phys. Rev. B **97**, 020303(R) (2018).
 - ¹⁵ R. Ghosh, B. Mukherjee, and K. Sengupta, Phys. Rev. B **102**, 235114 (2020).
 - ¹⁶ D. V. Else, B. Bauer, and C. Nayak, Phys. Rev. Lett. **117**, 090402 (2016).
 - ¹⁷ B. Mukherjee, S. Nandy, A. Sen, D. Sen, and K. Sengupta, Phys. Rev. B **101**, 245107 (2020).
 - ¹⁸ B. Mukherjee, A. Sen, D. Sen, and K. Sengupta, Phys. Rev. B **102**, 014301 (2020).
 - ¹⁹ M. Basko, I. L. Aleiner, and B. L. Altshuler, Ann. Phys. **321**, 1126 (2006).
 - ²⁰ R. Nandkishore and D. Huse, Ann. Rev. Cond. Mat. **6**, 15 (2015).
 - ²¹ C. J. Turner, A. A. Michailidis, D. A. Abanin, M. Serbyn, and Z. Papić, Nat. Phys. **14**, 745 (2018); S. Maudgalya, N. Regnault, and B. A. Bernevig, Phys. Rev. B **98**, 235156 (2018).
 - ²² W. W. Ho, S. Choi, H. Pitchler, and M. D. Lukin, Phys. Rev. Lett. **122**, 040603 (2019); N. Shiraishi, J. Stat. Mech. **08313** (2019).
 - ²³ S. Choi, C. J. Turner, H. Pichler, W. W. Ho, A. A. Michailidis, Z. Papić, M. Serbyn, M. D. Lukin, and D. A. Abanin, Phys. Rev. Lett. **122**, 220603 (2019); T. Iadecola, M. Schecter, and S. Xu, Phys. Rev. B **100**, 184312 (2019).
 - ²⁴ P. A. McClarty, M. Haque, A. Sen and J. Richter, Phys. Rev. B **102**, 224303(2020); D. Banerjee and A. Sen Phys. Rev. Lett. **126**, 220601(2021).
 - ²⁵ A. Chandran, T. Iadecola, V. Khemani, R. Moessner, arXiv:2206.11528 (unpublished).
 - ²⁶ S. Sugiura, T. Kuwahara, and K. Saito, Phys. Rev. Research **3**, L012010 (2021); P-G Rozon, M. J. Gullans, and K. Agarwal Phys. Rev. B **106**, 184304 (2022).
 - ²⁷ B. Mukherje, A. Sen, and K. Sengupta, Phys. Rev. B **106**, 064305 (2022); A. Hudomal, J-Y Desaulles, B. Mukherjee, G-X Su, J. C. Halimeh, and Z. Papic, Phys. Rev. B **106**, 104302 (2022).
 - ²⁸ V. Khemani, M. Hermele and R. Nandkishore, Phys. Rev.

- B **101**, 174204 (2020).
- ²⁹ P. Sala, T. Rakovszky, R. Verresen, M. Knap and F. Pollmann, Phys. Rev. X **10**, 011047 (2020).
- ³⁰ T. Rakovszky, P. Sala, R. Verresen, M. Knap and F. Pollmann, Phys. Rev. B **101**, 125126 (2020).
- ³¹ Z.-C. Yang, F. Liu, A. V. Gorshkov and T. Iadecola, Phys. Rev. Lett. **124**, 207602 (2020).
- ³² G. De Tomasi, D. Hetterich, P. Sala, and F. Pollmann, Phys. Rev. B **100**, 214313(2019); P. Frey, L. Hackl, and S. Rachel, arXiv:2209.11777 (unpublished).
- ³³ S. Moudgalya and O. I. Motrunich, Phys. Rev. X **12**, 011050 (2022); D. T. Stephen, O. Hart, and R. M. Nandkishore, arXiv:2209.03966 (unpublished); D. Hahn, P. A. McClarty, D. J. Luitz, SciPost Phys. **11**, 074 (2021); N. Regnault and B. A. Bernevig, arXiv:2210.08019 (unpublished).
- ³⁴ T. Kohlert, S. Scherg, P. Sala, F. Pollmann, B. H. Madhusudhana, I. Bloch, and M. Aidelsburger, arXiv:2106.15586 (unpublished).
- ³⁵ B. Mukherjee, D. Banerjee, K. Sengupta, and A. Sen, Phys. Rev. B **104**, 155117 (2021); P. Brighi, M. Ljubotina, and M. Serbyn, arXiv:2210.5607 (unpublished).
- ³⁶ J. Lehmann, P. Sala, F. Pollmann, and T. Rakovszky arXiv:2208.12260 (unpublished).
- ³⁷ A. Chattopadhyay, B. Mukherjee, K. Sengupta, and A. Sen, arXiv:2208.13800 (unpublished).
- ³⁸ D. N. Page, Phys. Rev. Lett. **71**, 1291 (1993); L. Vidmar and M. Rigol, Phys. Rev. Lett. **119**, 220603 (2017).
- ³⁹ P. Mazur, Physica **43**, 533 (1969); J. Sirker, SciPost Phys. Lect. Notes **17**, 1 (2020).
- ⁴⁰ See supplementary information for details.
- ⁴¹ A. Sen, D. Sen, and K. Sengupta, J. Phys. Cond. Mat. **33**, 443003 (2021).
- ⁴² A. Soori and D. Sen, Phys. Rev. B **82**, 115432 (2010).
- ⁴³ T. Bilitewski and N. Cooper, Phys. Rev. A **91**, 063611 (2015).
- ⁴⁴ T. Mori, T. Kuwahara, and K. Saito. Phys. Rev. Lett. **116**, 120401 (2016); T. Kuwahara, T. Mori, and K. Saito, Annals of Physics **367**, 96 (2016).
- ⁴⁵ S. Vajna, K. Klobas, T. Prosen, and A. Polkovnikov, Phys. Rev. Lett. **120**, 200607 (2018).
- ⁴⁶ I. Bloch, J. Dalibard, and W. Zwerger, Rev. Mod. Phys. **80**, 885 (2008).